

# RSC Advances



This is an *Accepted Manuscript*, which has been through the Royal Society of Chemistry peer review process and has been accepted for publication.

*Accepted Manuscripts* are published online shortly after acceptance, before technical editing, formatting and proof reading. Using this free service, authors can make their results available to the community, in citable form, before we publish the edited article. This *Accepted Manuscript* will be replaced by the edited, formatted and paginated article as soon as this is available.

You can find more information about *Accepted Manuscripts* in the [Information for Authors](#).

Please note that technical editing may introduce minor changes to the text and/or graphics, which may alter content. The journal's standard [Terms & Conditions](#) and the [Ethical guidelines](#) still apply. In no event shall the Royal Society of Chemistry be held responsible for any errors or omissions in this *Accepted Manuscript* or any consequences arising from the use of any information it contains.



Journal Name

ARTICLE

## Synthesis of Graphene Wrapped ZnMn<sub>2</sub>O<sub>4</sub> Hollow Microspheres as High Performance Anode Materials for Lithium Ion Batteries

Tong Zhang<sup>[a]</sup>, Huijuan Yue<sup>[b]</sup>, Hailong Qiu<sup>[a]</sup>, Kai Zhu<sup>[a]</sup>, Lijie Zhang<sup>[a]</sup>, Yingjin Wei<sup>[a]</sup>, Fei Du<sup>[a]</sup>, Gang Chen<sup>[a][c]</sup>, and Dong Zhang<sup>[a]\*</sup>

Received 00th January 20xx,  
Accepted 00th January 20xx

DOI: 10.1039/x0xx00000x

www.rsc.org/

Hollow microspheres of ZnMn<sub>2</sub>O<sub>4</sub> wrapped by graphene have been successfully synthesized via a facile ATPMS aid method. Characterization results certify that the reduced graphene sheets have been wrapped on the hollow ZnMn<sub>2</sub>O<sub>4</sub> microspheres. Charge–discharge testing reveals that ZnMn<sub>2</sub>O<sub>4</sub>/RGO serves superior electrochemical properties in terms of specific capacity, cycle stability (1082 mA h g<sup>-1</sup> at 100 mA g<sup>-1</sup> after 90 cycles) and high rate capability (580 mA h g<sup>-1</sup> at 1 A g<sup>-1</sup> after 150 cycles). The improved rate capability and cycling performance of the modified ZnMn<sub>2</sub>O<sub>4</sub> are attributed to the incorporated RGO sheets perfect synergy collaborate with hollow structure that can provide higher electronic conductivity, more Li<sup>+</sup> transmission path and also buffer the volume change during Li<sup>+</sup> insertion and extraction.

### Introduction

Energy storage devices have attracted great attention due to the increasing demands for sustainable and renewable energy owing to the limited supply of fossil fuels and environmental problems. Therefore rechargeable lithium-ion batteries with high storage capacity and cycling stability are considered to be versatile, clean and promising power sources.<sup>1–6</sup> Over the years, metal oxides, such as nickel oxides, cobalt oxides, iron oxides and tin oxides, have been considered as potential substitutes for the traditional graphite anode due to their higher theoretical specific capacities (600~1000 mAh g<sup>-1</sup>).<sup>7–12</sup> Recently, ZnMn<sub>2</sub>O<sub>4</sub> with a spinel structure has been found to possess obvious advantages because of its less cost, toxicity and lower working voltage (as a general rule, anode materials with lower charge/discharge voltages versus Li/Li<sup>+</sup> can deliver a higher energy density).<sup>13, 14</sup> In consequences, ZnMn<sub>2</sub>O<sub>4</sub> has attracted much attention as a high performance anode material for lithium-ion batteries.<sup>15–18</sup> However, the crucial problems of the material are the poor cycle ability and rate performance during Li ion insertion and extraction due to the large volume change induced electrode pulverization and its poor electronic conductivity.<sup>19, 20</sup> Therefore, developing high performance ZnMn<sub>2</sub>O<sub>4</sub> electrode material with both outstanding cycling stability and rate capability remains a great challenge. As we known, the introduction of conductive interconnected networks is one of the most common approaches to promote the electrical conductivity, leading to

enhance the electrochemical performance of electrode materials. For instance, Yin et al. synthesized the ZnMn<sub>2</sub>O<sub>4</sub>/carbon aerogel hybrid, which displayed a reversible capacity of 833 mAh g<sup>-1</sup> at a current density of 100 mA g<sup>-1</sup>.<sup>21</sup> Li et al. reported that the 3D ZnMn<sub>2</sub>O<sub>4</sub>/PCF exhibited a high capacity of 760 mAh g<sup>-1</sup> at 100 mA g<sup>-1</sup> and superior rate capability.<sup>22</sup>

Graphene is a two-dimensional mono-atomic thick lattice of carbon atoms. It has excellent electronic conductivity, large specific surface area and chemical stability.<sup>23</sup> To date, great progress has been obtained for synthesis of graphene modified materials for lithium ion batteries.<sup>24–26</sup> The superior electrochemical performance is due to a three-dimensional conductive network offered by graphene substrate. Furthermore, graphene can be used as a "buffer backbone" to support the electrode material and slow down the electrode pulverization, thus suppressing the capacity fading to a certain extent.<sup>27–29</sup> Recently, various of hybrid ZnMn<sub>2</sub>O<sub>4</sub>/graphene composites have been reported, such as ZnMn<sub>2</sub>O<sub>4</sub> nanoparticles/graphene,<sup>30</sup> ZnMn<sub>2</sub>O<sub>4</sub> nanorods/graphene,<sup>31</sup> ZnMn<sub>2</sub>O<sub>4</sub> porous spheres/graphene.<sup>32</sup> As expected, a high reversible capacity and excellent rate capability are achieved. Comparing to other morphologies, hollow microspheres exhibit their unique advantages on increasing the electrolyte-materials contact area, buffering the large volume change and alleviating the strain caused during repeated Li<sup>+</sup> insertion/extraction, thus improving the cycling stability and rate capability. Right now, series of anode materials in hollow spherical architectures with improved capacity and cycle performances have been explored.<sup>5, 33–37</sup>

Herein, in order to obtain an improved electrochemical performance of ZnMn<sub>2</sub>O<sub>4</sub> anode, we report a method to prepare hollow ZnMn<sub>2</sub>O<sub>4</sub> microspheres supported by reduced graphene oxide (RGO). Compared with the pure ZnMn<sub>2</sub>O<sub>4</sub>

<sup>a</sup> Key Laboratory of Physics and Technology for Advanced Batteries (Ministry of Education), College of Physics, Jilin University, Changchun 130012 (P. R. China).

<sup>b</sup> State Key Laboratory of Inorganic Synthesis and Preparative Chemistry, College of Chemistry, Jilin University, Changchun 130012 (P. R. China).

<sup>c</sup> State Key Laboratory of Superhard Materials, Jilin University, Changchun 130012 (P. R. China).

material, the  $\text{ZnMn}_2\text{O}_4/\text{RGO}$  composite exhibits higher reversible capacity and enhanced rate capability. It is due to the synergistic effect of the stable hollow structures and graphene nanosheets on the accommodation of volume change, the reduction of the diffusion path of lithium ions and the enhancement of electronic conductivity.

## Experimental

### Synthesis of $\text{ZnMn}_2\text{O}_4$ hollow microspheres

0.5948 g  $\text{Zn}(\text{NO}_3)_2 \cdot 6\text{H}_2\text{O}$ , 1.4316 g  $\text{Mn}(\text{NO}_3)_2 \cdot 4\text{H}_2\text{O}$ , and 0.42028 g citric acid were dissolved in a solution consisting of 9 mL deionized water and 25 mL ethanol. The solution, after being magnetically stirred for 10 min in air at room temperature, was transferred to a 50 mL Teflon-lined stainless steel autoclave. The autoclave was then tightly sealed and left in an oven at  $140^\circ\text{C}$  for 6 h. After reaction, the autoclave was cooled to room temperature naturally. The products were obtained by centrifuging and sequentially washing with water and ethanol for several times and then dried in a vacuum oven at  $60^\circ\text{C}$  for 10 h.

### Synthesis of RGO modified $\text{ZnMn}_2\text{O}_4$ hollow microspheres

The GO suspension was prepared from natural graphite by a modified Hummers method, as reported elsewhere.<sup>38</sup> To prepare the RGO modified  $\text{ZnMn}_2\text{O}_4$  hollow microspheres, typically, 0.4 g  $\text{ZnMn}_2\text{O}_4$  hollow microspheres were dispersed into 250 mL ethanol. Then, 8 mL of 3-aminopropyltrimethoxysilane (APS) was added, and refluxed at  $80^\circ\text{C}$  for 10 h, followed by sufficient wash with ethanol. Afterwards, the APS-treated  $\text{ZnMn}_2\text{O}_4$  hollow microspheres were added into a certain amount of graphene oxide (GO) suspension under sonication. The suspension was then washed with deionized water and dried at  $70^\circ\text{C}$  overnight. Finally, the  $\text{ZnMn}_2\text{O}_4/\text{RGO}$  composite was obtained by annealing the as prepared powder at  $350^\circ\text{C}$  for 3 h in air. The possible evolution process is illustrated in Fig. 1.

### Sample characterization

X-ray diffraction (XRD) of the samples was measured on a Bruker AXS D8 X-ray diffractometer using  $\text{Cu-K}\alpha$  X-ray source operating at 40 kV and 100 mA. The diffraction data was recorded in the  $2\theta$  range of  $10\text{--}80^\circ$  with a scan rate of  $5^\circ/\text{min}$ . The elemental analysis was carried out on an Elementar Vario EL cube. X-ray photoelectron spectroscopy (XPS) test was performed on an ESCALAB spectrometer with  $\text{Mg-K}\alpha$  light source. The morphology of the material was studied with a JSM-6700F scanning electron microscope (SEM). Transmission electron microscope (TEM) and high-resolution TEM (HRTEM) images were taken on an FEI Tacnai G2 electron microscope operated at 200 kV. Raman scattering spectroscopy was recorded on a Renishaw inVia Raman microscope with Ar-ion laser excitation ( $\lambda = 663\text{ nm}$ ).

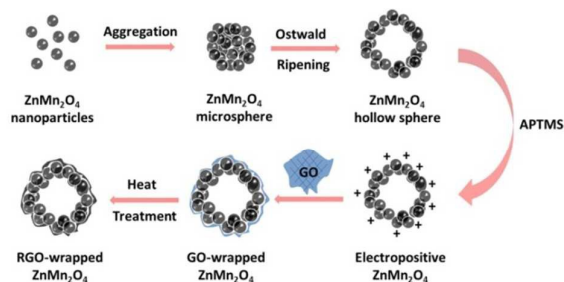


Fig. 1 Schematic of the formation mechanism of  $\text{ZnMn}_2\text{O}_4/\text{RGO}$ .

### Electrochemical measurements

The electrochemical characterization was performed using 2032-type coin cells while using metallic lithium foil as the counter electrode. The working electrode was composed of 80 wt.% of active material, 10 wt.% of super P (Sinopharm) conductive additive and 10 wt.% of CMC (Sigma-Aldrich)–SBR (NIPPON A&L INC) (CMC:SBR = 1:1 by weight ratio) binder, which was then pasted onto a copper current collector and cutting into pieces of  $1\text{ cm} \times 1\text{ cm}$ . The loading mass of active material was about  $1\text{--}2\text{ mg}/\text{cm}^2$ . The counter electrode and working electrode were separated by Celgard 2320 membrane. A 1 mol/L  $\text{LiPF}_6$  (lithium hexafluorophosphate) solution dissolved in EC (ethylene carbonate), DMC (dimethyl carbonate) (EC: DMC = 3:7) was used as the electrolyte. The battery cells were assembled in an argon-filled glove box. The charge-discharge test was measured on a LAND-2100 (Wuhan, China) battery tester in the voltage between 0.01–3.0 V versus  $\text{Li}/\text{Li}^+$ . Electrochemical impedance spectroscopy (EIS) and cyclic voltammetry (CV) were performed on a VSP multichannel galvanostatic-potentiostatic system (Bio-Logic SAS, France). The impedance spectra were carried out by applying an *ac* voltage of 5 mV in the frequency range from 1 MHz to 5 mHz.

## Results and discussion

### Structure and morphology analysis

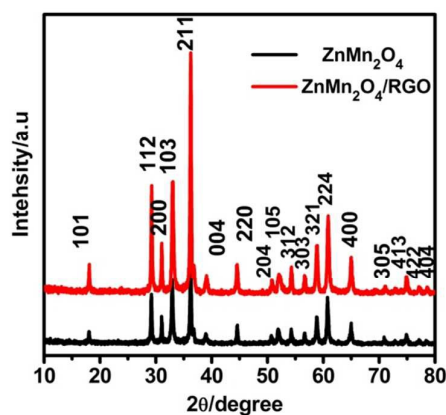


Fig. 2 XRD patterns of  $\text{ZnMn}_2\text{O}_4/\text{RGO}$  and  $\text{ZnMn}_2\text{O}_4$ .

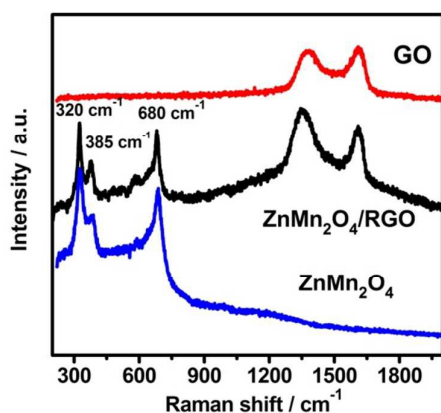


Fig. 3 Raman spectra of  $\text{ZnMn}_2\text{O}_4$ ,  $\text{ZnMn}_2\text{O}_4/\text{RGO}$  and GO.

Fig. 2 shows the XRD patterns of the  $\text{ZnMn}_2\text{O}_4$  and  $\text{ZnMn}_2\text{O}_4/\text{RGO}$  samples. The materials can be indexed well on the basis of tetragonal structure of  $\text{ZnMn}_2\text{O}_4$  with space group of  $I4_1/amd$  (JCPDS card No. 14-7311). The lattice parameters of both samples are the same despite of modifying ( $a = 5.720 \text{ \AA}$  and  $c = 9.243 \text{ \AA}$ ), which are consistent well with the literature<sup>21, 39</sup> and the values given in the standard card. Similar average crystallite size of  $\text{ZnMn}_2\text{O}_4$  and  $\text{ZnMn}_2\text{O}_4/\text{RGO}$  samples are calculated as about 30 nm from the (2 1 1) reflection according to the Scherrer formula  $D = k\lambda/\beta \cos \theta$ ,<sup>40</sup> where  $\beta$  is the angular line width at half of the maximum intensity in the (2 1 1) crystal facet,  $\lambda$  is the wavelength of the X-ray radiation,  $K$  is a constant which is 0.9 and  $\theta$  is the Bragg angle. There are no visible impurities present, indicating the formation of highly pure  $\text{ZnMn}_2\text{O}_4$  compound. It is noticed that no typical diffraction peak of GO (001) (normally appears at  $10^\circ$ ) or graphene (002) (normally appears at  $26.5^\circ$ ) can be observed in the XRD pattern of the  $\text{ZnMn}_2\text{O}_4/\text{RGO}$  composite which may be ascribed to the fact that GO was reduced to graphene during the heat treatment process and too small RGO content in the composite to be detected by XRD.<sup>41</sup> The RGO content in the  $\text{ZnMn}_2\text{O}_4/\text{RGO}$  sample is determined to be merely 6.5 wt.% by the C/H/N elemental analysis.

Fig. 3 shows the Raman spectra of the as-synthesized  $\text{ZnMn}_2\text{O}_4$ , GO and  $\text{ZnMn}_2\text{O}_4/\text{RGO}$  samples. As we can see, both  $\text{ZnMn}_2\text{O}_4$  and  $\text{ZnMn}_2\text{O}_4/\text{RGO}$  exhibit three obvious peaks located at  $320 \text{ cm}^{-1}$ ,  $385 \text{ cm}^{-1}$  and  $680 \text{ cm}^{-1}$ , which are well consistent with the characteristic vibration modes of  $\text{ZnMn}_2\text{O}_4$  reported in the literatures.<sup>42-46</sup> In the cubic spinel oxides, the modes above  $600 \text{ cm}^{-1}$  are usually correspond to the motion of oxygen in the tetrahedral  $\text{AO}_4$  group with  $A_{1g}$  symmetry.<sup>47</sup> The other two low frequency modes are characteristics of the octahedral site ( $\text{BO}_6$ ).<sup>48,49</sup> Two additional Raman bands at  $1356 \text{ cm}^{-1}$  and  $1603 \text{ cm}^{-1}$  associated with the disordered (D) and graphitic (G) bands of carbon-based materials are present in the spectrum of  $\text{ZnMn}_2\text{O}_4/\text{RGO}$  sample. The intensity ratio of the D-to-G bands is usually an indication of graphitization degree in carbon-based materials. A larger D-to-G intensity ratio of  $\text{ZnMn}_2\text{O}_4/\text{RGO}$  compared with that of GO strongly suggests the

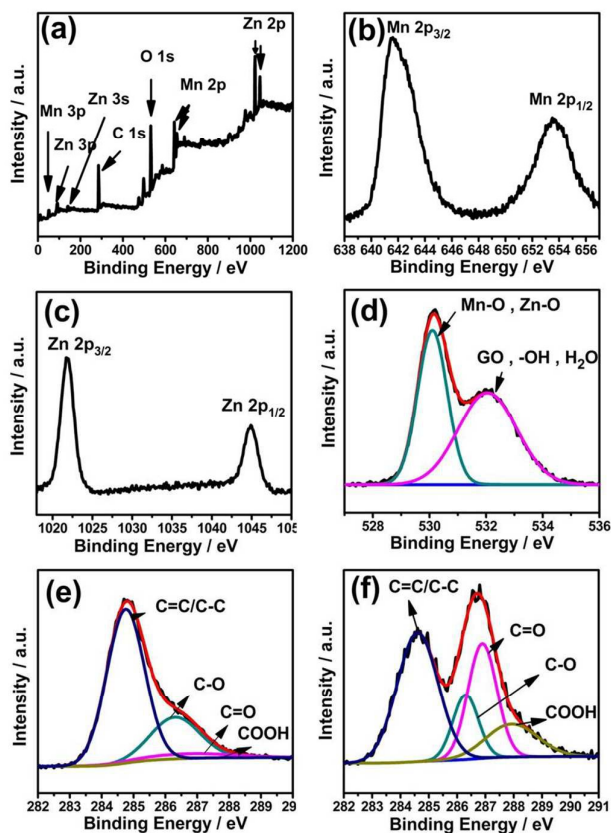


Fig. 4 XPS survey spectrum of the  $\text{ZnMn}_2\text{O}_4/\text{RGO}$  composite (a), Mn 2p (b), Zn 2p (c), O 1s (d) and C 1s spectrum of the  $\text{ZnMn}_2\text{O}_4/\text{RGO}$  composite (e), C 1s spectrum of GO (f).

reduction of GO to graphene,<sup>29, 50</sup> caused by the increased number of defects and edges generated during the heat treatment process.

The XPS analysis reveals the surface composition and chemical state of  $\text{ZnMn}_2\text{O}_4/\text{RGO}$ . The survey spectrum of Fig. 4(a) shows that the sample consists of manganese, zinc, oxygen, and carbon elements.<sup>51</sup> The Mn 2p spectrum shown in Fig. 4(b) exhibits two peaks at binding energy of 653.6 and 641.8 eV corresponding to Mn  $2p_{1/2}$  and  $2p_{3/2}$ , respectively. This characteristic indicates the oxidation state of Mn in the  $\text{ZnMn}_2\text{O}_4/\text{RGO}$  to be  $\text{Mn}^{3+}$  and no signs of  $\text{Mn}^{2+}$  or  $\text{Mn}^{4+}$  ions detected.<sup>52, 53</sup> The peaks at binding energy of 1044.9 and 1021.7 eV in the Zn 2p spectrum shown in Fig. 4(c) are attributed to the Zn  $2p_{1/2}$  and Zn  $2p_{3/2}$ , respectively, demonstrating the presence of  $\text{Zn}^{2+}$  in the samples.<sup>54</sup> The wide and asymmetric O 1s spectrum can be fitted into two peaks, as shown in Fig. 4(d). One stronger peak with the binding energy of 530.2 eV implies the characteristics of lattice oxygen in metal (Mn, Zn) oxide. The peak of 532.2 eV indicates the contributions of the remanent unreduced GO and adsorbed oxygen, such as  $-\text{OH}$  and  $\text{H}_2\text{O}$  on the surface.<sup>54</sup> The C1s XPS spectra of  $\text{ZnMn}_2\text{O}_4/\text{RGO}$  and GO are given in Fig. 4 (e) and (f). The spectra of GO consists of four different peaks with binding energy centered at 284.6, 286.3, 287.0 and 288.1 eV, which can be attributed to graphitic C=C/C-C, C-O, C=O and COOH

bonds, respectively.<sup>38</sup> After reduction, the peaks from the oxygen-containing functional groups are significantly weakened which confirms the successful reduction of GO (Fig. 4(f)). Therefore, a good electrical conductivity is expected by undergoing this remarkable deoxygenation reaction.

Fig. 5(a) (b) and (c) shows the SEM image of the bare ZnMn<sub>2</sub>O<sub>4</sub> sample. The uniform microspheres with a diameter of 2-3 μm are detected and the hollow interior can be identified unambiguously from the broken part. Carefully observation on the surface of the spheres reveals that each sphere is consisted of spinel-like primary particles with sizes ranging from 100-200 nm. Similar size but less coarse surface of ZnMn<sub>2</sub>O<sub>4</sub> microspheres are shown in Fig. 5 (d) after they are embedded in RGO. Since the surface of GO was negatively charged in an aqueous solution, opposite to that of ZnMn<sub>2</sub>O<sub>4</sub>, a spontaneous assembly of the two components occurred upon mixing. The wrapping structure can be recognized from Fig. 5(e) and (f), where the RGO films are clearly seen to exist and fill the space of the material to effectively link the adjacent ZnMn<sub>2</sub>O<sub>4</sub> spheres. This connection can facilitate the transport of electrons in an effective percolating network and the contact area between the ZnMn<sub>2</sub>O<sub>4</sub> spheres as well thus gives rise to high electronic conductivity. The RGO sheets could not wrap over the surface of the ZnMn<sub>2</sub>O<sub>4</sub> spheres entirely due to the relatively large dimensions of the microspheres. TEM was used to further analyze the detailed structure information of ZnMn<sub>2</sub>O<sub>4</sub>/RGO sample. As shown in Fig. 6(a), it provide the best evidence for the hollow structure of the microspheres by showing notable contrast difference between the hollow and solid parts, and the RGO sheets are successfully wrapped on the surfaces of ZnMn<sub>2</sub>O<sub>4</sub> spheres. Fig. 6(b) shows the high magnification TEM image of the sphere edge where the RGO coating layer can be clearly distinguished. The thickness of the RGO layer is measured to be 5~20 nm that illustrates its multi-layer feature of graphene. Fig. 6(c) is a high resolution TEM (HRTEM) image recorded within the region marked by a rectangle in Fig. 6(a), indicating the amorphous state of the graphene and polycrystalline nature of the ZnMn<sub>2</sub>O<sub>4</sub> spheres. Lattice fringes with *d* spacing of 0.246 nm and 0.486 nm are observed, which is in consistent with the (211) and (101) interplanar spacings of the spinel ZnMn<sub>2</sub>O<sub>4</sub>.<sup>55, 56</sup> Hence, the presence of the flexible RGO wrapping layer on the ZnMn<sub>2</sub>O<sub>4</sub>

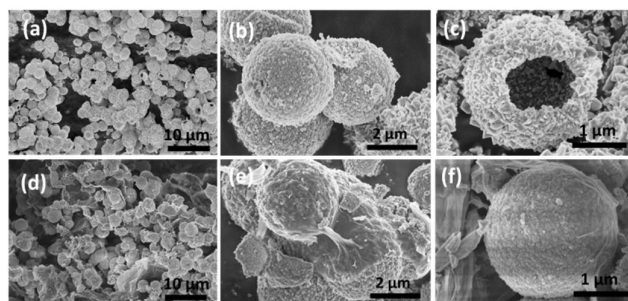


Fig. 5 SEM image of bare ZnMn<sub>2</sub>O<sub>4</sub> (a)(b)(c) and ZnMn<sub>2</sub>O<sub>4</sub>/RGO (d)(e)(f).

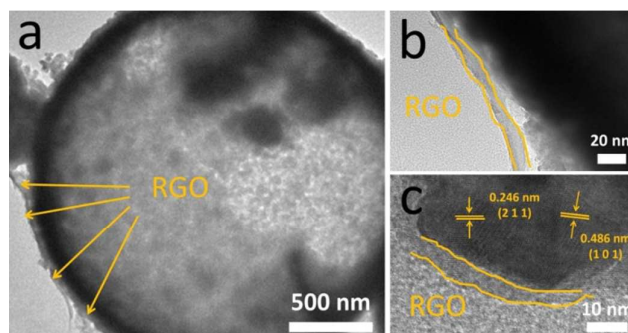
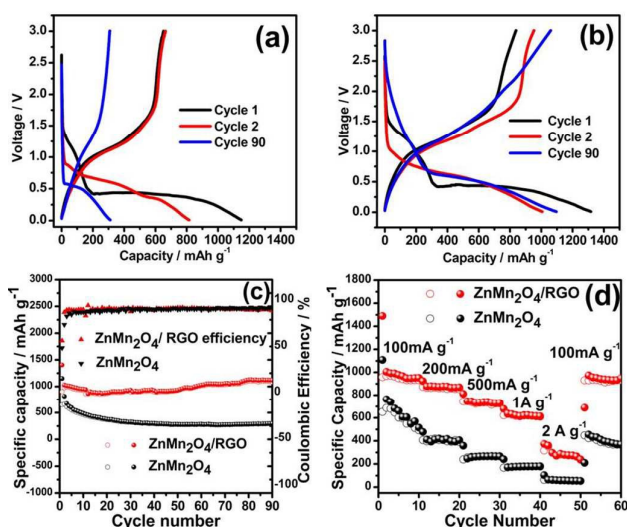


Fig. 6 TEM images of the ZnMn<sub>2</sub>O<sub>4</sub>/RGO composite (a, b), HRTEM images of the ZnMn<sub>2</sub>O<sub>4</sub>/RGO composite (c).

spheres can significantly improve the electronic conductivity of the material. DC electronic conductivity measurement shows that the electronic conductivity of the pristine ZnMn<sub>2</sub>O<sub>4</sub> is  $5.75 \times 10^{-11} \text{ S cm}^{-1}$  while the RGO wrapped ZnMn<sub>2</sub>O<sub>4</sub> is increased to  $8.55 \times 10^{-8} \text{ S cm}^{-1}$ , which is three orders of magnitude higher than that of the pristine material.

#### Electrochemical measurements

The discharge/charge curves of the ZnMn<sub>2</sub>O<sub>4</sub> and ZnMn<sub>2</sub>O<sub>4</sub>/RGO samples are shown in Fig. 7(a) and (b), which are recorded at a current density of  $100 \text{ mA g}^{-1}$  in the voltage range of 0.01 to 3.00 V (versus Li/Li<sup>+</sup>). The specific capacity of ZnMn<sub>2</sub>O<sub>4</sub>/RGO is calculated based on the total mass of ZnMn<sub>2</sub>O<sub>4</sub> and graphene. Despite their different specific capacities, both materials show similar discharge/charge curves indicating same electrochemical reactions occurring in the Li<sup>+</sup> insertion/de-insertions processes. In the first discharge step, there is a long and steady voltage plateau around 0.4 V which is replaced by a sloping curve in the following discharge, suggesting the reduction of ZnMn<sub>2</sub>O<sub>4</sub> to metallic Zn and Mn embedded in Li<sub>2</sub>O matrix and the formation of the Li-Zn alloy. The related reaction can be depicted as  $\text{ZnMn}_2\text{O}_4 + 9\text{Li}^+ + 9\text{e}^- \rightarrow \text{ZnLi} + 2\text{Mn} + 4\text{Li}_2\text{O}$ .<sup>57, 58</sup> For the subsequent discharge-charge process, the curves are quite similar and can be ascribed as  $\text{ZnLi} + 2\text{Mn} + 3\text{Li}_2\text{O} \leftrightarrow \text{ZnO} + 2\text{MnO} + 7\text{Li}^+ + 7\text{e}^-$ .<sup>32, 59</sup> However, both the two samples serve a higher practical capacity than the theoretical value in the first discharge stage which can be attributed to the formation of the solid electrolyte interface (SEI) film.<sup>13, 57, 60</sup> In addition, the first discharge and charge capacities of ZnMn<sub>2</sub>O<sub>4</sub>/RGO are 957 and 1346 mAh g<sup>-1</sup> with a coulombic efficiency of 71.1%, while those of bare ZnMn<sub>2</sub>O<sub>4</sub> are 650 and 1148 mAh g<sup>-1</sup>, and the coulombic efficiency is 56.7%. There are two probably reasons that lead the low coulombic efficiencies, one is the irreversible reaction during the first discharge process, while the other is the formation of a thick irreversible SEI layer on the surface of the material associated with the first cycle. Even though, we can obviously find that the participation of graphene considerably increases the charge/discharge capacities and boosts the initial coulombic efficiency of ZnMn<sub>2</sub>O<sub>4</sub>. The cycle performance of ZnMn<sub>2</sub>O<sub>4</sub> and ZnMn<sub>2</sub>O<sub>4</sub>/RGO samples is displayed in Fig. 7(c).



**Fig. 7** The charging–discharging curves of  $\text{ZnMn}_2\text{O}_4$  (a),  $\text{ZnMn}_2\text{O}_4/\text{RGO}$  (b), the corresponding cycling performances at a current density of  $100 \text{ mA g}^{-1}$  (c) and rate properties of  $\text{ZnMn}_2\text{O}_4$  and  $\text{ZnMn}_2\text{O}_4/\text{RGO}$  (d) at various current densities between 0.01 and  $3.0 \text{ V}$ .

Obviously, the bare  $\text{ZnMn}_2\text{O}_4$  exhibits gradual capacity fading with charge/discharge cycling. It only shows a discharge capacity of  $281 \text{ mAh g}^{-1}$  after 90 cycles, corresponding to a capacity retention of 43.2%. In comparison, the  $\text{ZnMn}_2\text{O}_4/\text{RGO}$  electrode shows excellent capacity retention. The material can still deliver a high discharge capacity of  $1082 \text{ mAh g}^{-1}$  after 50 cycles which is even better than that of the first cycle. The rate capability of the  $\text{ZnMn}_2\text{O}_4$  and  $\text{ZnMn}_2\text{O}_4/\text{RGO}$  materials are presented in Fig. 7(d), the  $\text{ZnMn}_2\text{O}_4/\text{RGO}$  electrode also exhibits greatly enhanced rate capability compared with the pure  $\text{ZnMn}_2\text{O}_4$  electrode. Even at a high current density of  $2 \text{ A g}^{-1}$ , the  $\text{ZnMn}_2\text{O}_4/\text{RGO}$  electrode can still deliver a reversible capacity of about  $280 \text{ mAh g}^{-1}$ , which is much higher than that of the pure  $\text{ZnMn}_2\text{O}_4$  ( $55 \text{ mAh/g}$ ). The high rate cycling performance of the  $\text{ZnMn}_2\text{O}_4/\text{RGO}$  composites were tested at the current density of  $1 \text{ A g}^{-1}$ . As shown in Fig. 8, the hybrid electrode shows an initial discharge specific capacity of  $844 \text{ mAh g}^{-1}$ , and the specific discharge capacity of this composite could still maintain at  $580 \text{ mAh g}^{-1}$  after 150 cycles. The superior electrochemical performance of  $\text{ZnMn}_2\text{O}_4/\text{RGO}$  can be attributed to the participation of graphene. Firstly, RGO sheets significantly improved the material electronic conductivity thus reducing the ohmic polarization of the electrode and resulting in good rate capability. Secondly, the large interface area of graphene provides more  $\text{Li}^+$  insertion/extraction sites which facilitate  $\text{Li}^+$  transfer between the electrode and the electrolyte, thus leading to a large reversible capacity. In addition the graphene nanosheets can work as an elastic buffer to accommodate larger volume expansion/contraction during  $\text{Li}^+$  insertion/de-insertion, thus leading to excellent cycling stability.

The morphologies of the pure  $\text{ZnMn}_2\text{O}_4$  and  $\text{ZnMn}_2\text{O}_4/\text{RGO}$  electrodes after 100<sup>th</sup> high rate cycling are investigated by SEM. As shown in Fig. 9(a) and (b), the electrode surface of  $\text{ZnMn}_2\text{O}_4$

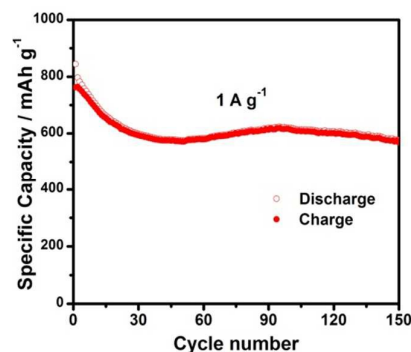


**Fig. 8** Cycling performance of  $\text{ZnMn}_2\text{O}_4/\text{RGO}$  composites at  $1 \text{ A g}^{-1}$ .

exhibits some severe big gaps, while a dense and smooth surface film could be maintained in the cycled  $\text{ZnMn}_2\text{O}_4/\text{RGO}$  electrode, indicating its good maintainability during cycling. This is probably due to the strong cohesive force among the material particles offered by graphene substrate. From larger magnification images shown in Fig. 9(c) and (d), it is hardly to find integral spheres in  $\text{ZnMn}_2\text{O}_4$  electrode, and the gaps can be observed even clearer. As comparison, the spherical character has been maintained very well in the  $\text{ZnMn}_2\text{O}_4/\text{RGO}$  electrode. Above results are also the rational explanation of the enhanced cycle and rate performance of  $\text{ZnMn}_2\text{O}_4/\text{RGO}$  material.

AC impedance measurements were carried out in order to gain insight into the remarkable electrochemical performance of  $\text{ZnMn}_2\text{O}_4/\text{RGO}$ . Fig. 10(a) and (b) provides the Nyquist plots of the  $\text{ZnMn}_2\text{O}_4$  and  $\text{ZnMn}_2\text{O}_4/\text{RGO}$  samples collected at the open circuit voltage (OCV) and after three discharge/charge cycles. As shown in the figures, the impedance plots consist of a depressed semicircle as well as a straight line. It is well known that the intercept at the highest frequency is attributed to the internal resistance ( $R_s$ ) of the cell arising from the electrolyte, separator, current collector, etc. The semicircle in the middle frequency range is due to the charge-transfer resistance ( $R_{ct}$ ). The straight line in the low frequency (Warburg) is associated with lithium ion diffusion in the electrode bulk. Based on this,

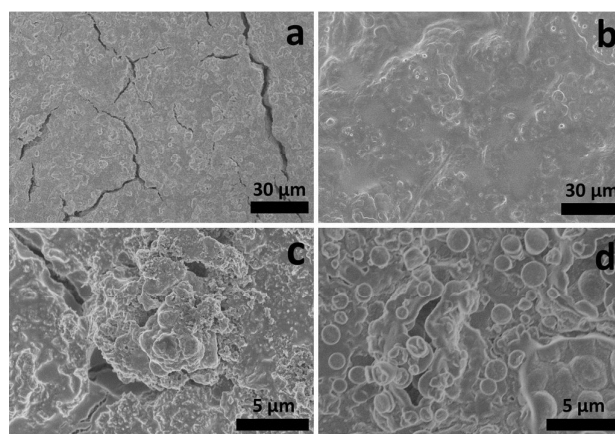


**Fig. 9** SEM images of the pure  $\text{ZnMn}_2\text{O}_4$  (a, c) and  $\text{ZnMn}_2\text{O}_4/\text{RGO}$  (b, d) electrodes after 100<sup>th</sup> high rate cycling.

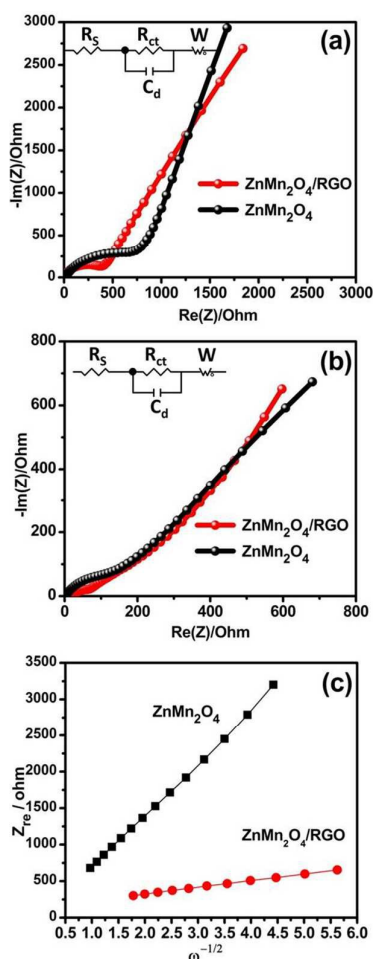


Fig. 10 Nyquist plots of ZnMn<sub>2</sub>O<sub>4</sub> and ZnMn<sub>2</sub>O<sub>4</sub>/RGO before cycling (a), after 3 cycles (b) by EIS measurement at 0.1 mV s<sup>-1</sup> and linear fit of the Z<sub>real</sub> versus ω<sup>-1/2</sup> relationship of ZnMn<sub>2</sub>O<sub>4</sub> and the ZnMn<sub>2</sub>O<sub>4</sub>/RGO composite (c).

the Nyquist plots are simulated using the equivalent circuit, as shown in the insets of Fig. 10(a) and (b). The Nyquist plots at the OCV state reflect the electrochemical kinetic properties of the block electrodes. It is seen that the ZnMn<sub>2</sub>O<sub>4</sub>/RGO electrode has a smaller semicircle (366.4 Ω) than the bare ZnMn<sub>2</sub>O<sub>4</sub> electrode (771 Ω). This indicates that the charge transfer resistance of the electrode is decreased by participant of RGO. The charge transfer resistance significantly decreases after three cycles due to the effective activation of the electrodes. One can see that the charge transfer resistance of ZnMn<sub>2</sub>O<sub>4</sub>/RGO (31.25 Ω) is still smaller than that of the bare ZnMn<sub>2</sub>O<sub>4</sub> electrode (139.4 Ω). This result validates that the RGO in ZnMn<sub>2</sub>O<sub>4</sub> microspheres enables lower charge transfer resistance and enhances the electrochemical activity of the ZnMn<sub>2</sub>O<sub>4</sub> active material.

The Warburg region in the Nyquist plots has been used to determine the chemical diffusion coefficient of Li<sup>+</sup> in electrode materials. By using the model proposed by Ho et al.,  $D_{Li}$  of ZnMn<sub>2</sub>O<sub>4</sub> and ZnMn<sub>2</sub>O<sub>4</sub>/RGO can be calculated by the equation:<sup>61</sup>

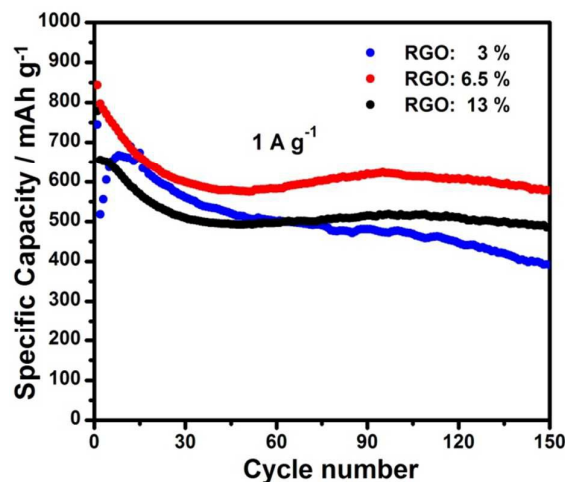


Fig. 11 Cycling performance of ZnMn<sub>2</sub>O<sub>4</sub>/RGO composites at various RGO content.

$$D_{Li} = 0.5 \left[ \left( \frac{V_m}{FS\sigma} \right) \frac{dE}{dx} \right] \quad (1)$$

Where  $V_m$  is the molar volume of ZnMn<sub>2</sub>O<sub>4</sub>,  $F$  is the Faraday constant,  $S$  is the active surface area of the electrode, and  $\frac{dE}{dx}$  is the first-order derivative of the discharge profile.  $\sigma$  is the Warburg factor which obeys the following relationship:

$$\sigma = \frac{dz'}{dw^{-1/2}} \quad (2)$$

Fig. 10 (c) displays the linear fitting of  $Z_{real}$  vs.  $\omega^{-1/2}$ , from which the slope  $\sigma$  can be obtained. Based on these, the chemical diffusion coefficients of ZnMn<sub>2</sub>O<sub>4</sub> and ZnMn<sub>2</sub>O<sub>4</sub>/RGO were calculated as  $1.362 \times 10^{-11} \text{ cm}^2 \text{ s}^{-1}$  and  $2.08 \times 10^{-11} \text{ cm}^2 \text{ s}^{-1}$ , respectively. The lithium diffusion coefficient  $D_{Li}$  is a transport parameter that reflects both the ionic and the electron transports of the active material. It is deduced from the Fick's first law and can be expressed as the product of a self-diffusion coefficient  $D_{Li(\text{self})}$  and a thermodynamic factor  $\Phi$ , i.e.,  $D_{Li} = D_{Li(\text{self})} \times \Phi$ .  $D_{Li(\text{self})}$  and  $\Phi$  are very sensitive to the structural and electronic properties of the material, respectively. Briefly,  $D_{Li(\text{self})}$  is a measure of the diffusion that takes place even in the absence of a chemical potential gradient and corresponds to the ionic mobility or viscosity in a solution. The  $\Phi$  factor measures the chemical potential deviation from that of an ideal solution. It depends on both kinetic parameters (transport number, mobility) and thermodynamic properties (stoichiometry, activity). Sometimes it indicates that the ionic flux density intensifies due to the simultaneous transport of electrons through the active material.<sup>62, 63</sup> As an intrinsic parameter of intercalation materials, the self-diffusion coefficient of ZnMn<sub>2</sub>O<sub>4</sub> should not be changed by GO wrapping. Thus, the larger lithium diffusion coefficient of ZnMn<sub>2</sub>O<sub>4</sub>/RGO should be closely related with the higher electronic conductivity. The enhancement of electronic conductivity, no matter the intrinsic electronic conductivity or the surface electronic conductivity, will lower the internal resistance of the

electrode, and therefore increase the internal electrical field inside the battery. As a result, the diffusion of Li ions is accelerated by this stronger internal electrical field thus resulting in higher lithium diffusion coefficient.

To consummate our investigation, the high rate electrochemical tests of ZnMn<sub>2</sub>O<sub>4</sub>/RGO with various RGO content have been carried out. As displayed in Fig. 11, the result verifies again that incorporation of RGO indeed improves the electrochemical performance of ZnMn<sub>2</sub>O<sub>4</sub>. Moreover, appropriate amount of RGO is helpful to significantly improve the electrochemical performance of ZnMn<sub>2</sub>O<sub>4</sub>.

## Conclusions

In summary, we presented a facile synthetic approach to fabricate the spinel ZnMn<sub>2</sub>O<sub>4</sub>/RGO hollow microspheres. As expected, the ZnMn<sub>2</sub>O<sub>4</sub>/RGO shows improved capacity, cycling stability and rate capability compared to bare ZnMn<sub>2</sub>O<sub>4</sub>. The superior performance of the ZnMn<sub>2</sub>O<sub>4</sub>/RGO is due to the synergetic effect between the conducting graphene nanosheets and ZnMn<sub>2</sub>O<sub>4</sub> hollow microspheres. The unique carbon framework not only provides an expressway for electron transfer during Li<sup>+</sup> insertion/de-insertion, but also improves the lithium diffusion in the electrode bulk. The good electrochemical properties of ZnMn<sub>2</sub>O<sub>4</sub>/RGO make it a promising anode material for Li-ion batteries.

## Acknowledgements

This study was supported by the National Natural Science Foundation of China (No. 51272088 and 21201073), the Science and Technology Development Planning of Jilin Province (No. 20150204030GX), the graduate Innovation Fund of Jilin University Project (No. 2015012).

## Notes and references

- P. Poizot and F. Dolhem, *Energy & Environmental Science*, 2011, **4**, 2003.
- Y. Wang and G. Cao, *Advanced materials*, 2008, **20**, 2251-2269.
- H. Xia, Y. Qian, Y. Fu and X. Wang, *Solid State Sciences*, 2013, **17**, 67-71.
- P. G. Bruce, B. Scrosati and J.-M. Tarascon, *Angewandte Chemie International Edition*, 2008, **47**, 2930-2946.
- G. Wang, R. Chen, Y. Zhou, H. Wang and J. Bai, *Journal of Nanoparticle Research*, 2014, **16**.
- O. K. Park, Y. Cho, S. Lee, H.-C. Yoo, H.-K. Song and J. Cho, *Energy & Environmental Science*, 2011, **4**, 1621.
- Z. Zheng, Y. Cheng, X. Yan, R. Wang and P. Zhang, *Journal of Materials Chemistry A*, 2014, **2**, 149.
- Z. Wang, L. Zhou and X. W. David Lou, *Advanced materials*, 2012, **24**, 1903-1911.
- B. Wang, J. S. Chen, H. B. Wu, Z. Wang and X. W. Lou, *Journal of the American Chemical Society*, 2011, **133**, 17146-17148.
- M. V. Reddy, T. Yu, C. H. Sow, Z. X. Shen, C. T. Lim, G. V. Subba Rao and B. V. R. Chowdari, *Advanced Functional Materials*, 2007, **17**, 2792-2799.
- Z. Li, G. Wu, D. Liu, W. Wu, B. Jiang, J. Zheng, Y. Li, J. Li and M. Wu, *J. Mater. Chem. A*, 2014, **2**, 7471-7477.
- M. Wu, J. Liu, M. Tan, Z. Li, W. Wu, Y. Li, H. Wang, J. Zheng and J. Qiu, *RSC Adv.*, 2014, **4**, 25189-25194.
- Y. Yang, Y. Zhao, L. Xiao and L. Zhang, *Electrochemistry Communications*, 2008, **10**, 1117-1120.
- S.-W. Kim, H.-W. Lee, P. Muralidharan, D.-H. Seo, W.-S. Yoon, D. K. Kim and K. Kang, *Nano Research*, 2011, **4**, 505-510.
- Y. Deng, S. Tang, Q. Zhang, Z. Shi, L. Zhang, S. Zhan and G. Chen, *Journal of Materials Chemistry*, 2011, **21**, 11987.
- J. G. Kim, S. H. Lee, Y. Kim and W. B. Kim, *ACS Applied Materials & Interfaces*, 2013, **5**, 11321-11328.
- Y.-S. Park, H. Oh and S.-M. Lee, *Bulletin of the Korean Chemical Society*, 2011, **32**, 3333-3337.
- P. F. Teh, Y. Sharma, Y. W. Ko, S. S. Pramana and M. Srinivasan, *RSC Advances*, 2013, **3**, 2812.
- L. Yao, X. Hou, S. Hu, Q. Ru, X. Tang, L. Zhao and D. Sun, *Journal of Solid State Electrochemistry*, 2013, **17**, 2055-2060.
- L. Xiao, Y. Yang, J. Yin, Q. Li and L. Zhang, *Journal of Power Sources*, 2009, **194**, 1089-1093.
- L. Yin, Z. Zhang, Z. Li, F. Hao, Q. Li, C. Wang, R. Fan and Y. Qi, *Advanced Functional Materials*, 2014, **24**, 4176-4185.
- P. Li, J. Liu, Y. Liu, Y. Wang, Z. Li, W. Wu, Y. Wang, L. Yin, H. Xie, M. Wu, X. He and J. Qiu, *Electrochimica Acta*, 2015, **180**, 164-172.
- A. K. Geim, *Science*, 2009, **324**, 1530-1534.
- E. Yoo, J. Kim, E. Hosono, H.-s. Zhou, T. Kudo and I. Honma, *Nano Letters*, 2008, **8**, 2277-2282.
- G. Wang, X. Shen, J. Yao and J. Park, *Carbon*, 2009, **47**, 2049-2053.
- D. Chen, L. Tang and J. Li, *Chemical Society reviews*, 2010, **39**, 3157-3180.
- Q. Fan, L. Lei, X. Xu, G. Yin and Y. Sun, *Journal of Power Sources*, 2014, **257**, 65-69.
- X. L. Chen, B. Cheng, H. Y. Xu, J. Yang and Y. T. Qian, *Chemistry Letters*, 2012, **41**, 639-641.
- W. Song, J. Xie, S. Liu, G. Cao, T. Zhu and X. Zhao, *New Journal of Chemistry*, 2012, **36**, 2236.
- P. Xiong, B. Liu, V. Teran, Y. Zhao, L. Peng, X. Wang and G. Yu, *ACS Nano*, 2014, **8**, 8610-8616.
- Z. Zheng, Y. Cheng, X. Yan, R. Wang and P. Zhang, *Journal of Materials Chemistry A*, 2014, **2**, 149.
- D. Cai, D. Wang, H. Huang, X. Duan, B. Liu, L. Wang, Y. Liu, Q. Li and T. Wang, *Journal of Materials Chemistry A*, 2015, **3**, 11430-11436.
- M. Zhao, B. Cai, Y. Ma, H. Cai, J. Huang, X. Pan, H. He and Z. Ye, *Biosensors and Bioelectronics* 6.451, 2014, **61**, 443-447.
- L. Zhou, H. B. Wu, T. Zhu and X. W. Lou, *Journal of Materials Chemistry*, 2012, **22**, 827.
- G. Zhang, L. Yu, H. B. Wu, H. E. Hoster and X. W. Lou, *Advanced materials*, 2012, **24**, 4609-4613.
- G. Zhang and X. W. D. Lou, *Angewandte Chemie International Edition*, 2014, **53**, 9041-9044.
- J. Li, S. Xiong, X. Li and Y. Qian, *Nanoscale*, 2013, **5**, 2045-2054.
- L. Yang, J. Kong, W. A. Yee, W. Liu, S. L. Phua, C. L. Toh, S. Huang and X. Lu, *Nanoscale*, 2012, **4**, 4968.
- N. Wang, X. Ma, H. Xu, L. Chen, J. Yue, F. Niu, J. Yang and Y. Qian, *Nano Energy*, 2014, **6**, 193-199.
- H. Yin, Y. Wada, T. Kitamura, S. Kambe, S. Murasawa, H. Mori, T. Sakata and S. Yanagida, *Journal of Materials Chemistry*, 2001, **11**, 1694-1703.
- X. Yan, Y. Li, F. Du, K. Zhu, Y. Zhang, A. Su, G. Chen and Y. Wei, *Nanoscale*, 2014, **6**, 4108.
- H. Li, B. Song, W. J. Wang and X. L. Chen, *Materials Chemistry and Physics*, 2011, **130**, 39-44.

- 43 L. Malavasi, P. Galinetto, M. C. Mozzati, C. B. Azzoni and G. Flor, *Physical Chemistry Chemical Physics*, 2002, **4**, 3876-3880.
- 44 B. Hadžić, N. Romčević, M. Romčević, I. Kuryliszyn-Kudelska, W. Dobrowolski, R. Wróbel, U. Narkiewicz and D. Sibera, *Journal of Alloys and Compounds*, 2014, **585**, 214-219.
- 45 F. Rubio-Marcos, A. Quesada, M. A. García, M. A. Bañares, J. L. G. Fierro, M. S. Martín-Gonzalez, J. L. Costa-Krämer and J. F. Fernández, *Journal of Solid State Chemistry*, 2009, **182**, 1211-1216.
- 46 K. Samanta, S. Dussan, R. S. Katiyar and P. Bhattacharya, *Applied Physics Letters*, 2007, **90**, 261903.
- 47 Y. Qu, H. Yang, N. Yang, Y. Fan, H. Zhu and G. Zou, *Materials Letters*, 2006, **60**, 3548-3552.
- 48 Z. Wang, R. T. Downs, V. Pischedda, R. Shetty, S. K. Saxena, C. S. Zha, Y. S. Zhao, D. Schiferl and A. Waskowska, *Physical Review B*, 2003, **68**, 094101.
- 49 L. V. Gasparov, D. B. Tanner, D. B. Romero, H. Berger, G. Margaritondo and L. Forró, *Physical Review B*, 2000, **62**, 7939-7944.
- 50 S. Stankovich, D. A. Dikin, R. D. Piner, K. A. Kohlhaas, A. Kleinhammes, Y. Jia, Y. Wu, S. T. Nguyen and R. S. Ruoff, *Carbon*, 2007, **45**, 1558-1565.
- 51 P. Zhang, X. Li, Q. Zhao and S. Liu, *Nanoscale Research Letters*, 2011, **6**, 323.
- 52 J. F. Fernández, A. C. Caballero, M. Villegas, S. J. Khatib, M. A. Bañares, J. L. G. Fierro, J. L. Costa-Kramer, E. Lopez-Ponce, M. S. Martín-González, F. Briones, A. Quesada, M. García and A. Hernando, *Journal of the European Ceramic Society*, 2006, **26**, 3017-3025.
- 53 X. F. Chen, L. Qie, L. L. Zhang, W. X. Zhang and Y. H. Huang, *Journal of Alloys and Compounds*, 2013, **559**, 5-10.
- 54 L. Xue, Z.-S. Wu, C. Ge and X.-D. Zhang, *Materials Chemistry and Physics*, 2013, **138**, 124-130.
- 55 C. Yuan, L. Zhang, S. Zhu, H. Cao, J. Lin and L. Hou, *Nanotechnology*, 2015, **26**, 145401.
- 56 M. H. Alfaruqi, A. K. Rai, V. Mathew, J. Jo and J. Kim, *Electrochimica Acta*, 2015, **151**, 558-564.
- 57 F. M. Courtel, Y. Abu-Lebdeh and I. J. Davidson, *Electrochimica Acta*, 2012, **71**, 123-127.
- 58 L. Zhang, S. Zhu, H. Cao, G. Pang, J. Lin, L. Hou and C. Yuan, *RSC Advances*, 2015, **5**, 13667-13673.
- 59 X. Zeng, L. Shi, L. Li, J. Yang, X. Cheng and M. Gao, *RSC Advances*, 2015, **5**, 70379-70386.
- 60 D. Pasero, N. Reeves and A. West, *Journal of Power Sources*, 2005, **141**, 156-158.
- 61 C. Ho, I. D. Raistrick and R. A. Huggins, *Journal of The Electrochemical Society*, 1980, **127**, 343-350.
- 62 C. Wagner, *The Journal of Chemical Physics*, 1953, **21**, 1819.
- 63 L. A. Montoro, E. Y. Matsubara and J. M. Rosolen, *Journal of Power Sources*, 2014, **257**, 205-212.